The Astrophysical Journal Supplement Series, 169:75–82, 2007 March

SEARCH FOR POLARIZATION FROM THE PROMPT GAMMA-RAY EMISSION OF GRB 041219a WITH SPI ON *INTEGRAL*

E. Kalemci,[1] S. E. Boggs,[2,3] C. Kouveliotou,[4,5] M. Finger,[4,6] and M. G. Baring[7]

Received 2006 August 28; accepted 2006 October 27

ABSTRACT

Measuring the polarization of the prompt γ-ray emission from gamma-ray bursts (GRBs) can significantly improve our understanding of both the GRB emission mechanisms as well as the underlying engine driving the explosion. We searched for polarization in the prompt γ-ray emission of GRB 041219a with the SPI instrument on *INTEGRAL*. Using multiple-detector coincidence events in the 100–350 keV energy band, our analysis yields a polarization fraction from this GRB of $98\% \pm 33\%$. Statistically, we cannot claim a polarization detection from this source. Moreover, different event selection criteria lead to even less significant polarization fractions, e.g., lower polarization fractions are obtained when higher energies are included in the analysis. We cannot strongly rule out the possibility that the measured modulation is dominated by instrumental systematics. Therefore, SPI observations of GRB 041219a do not significantly constrain GRB models. However, this measurement demonstrates the capability of SPI to measure polarization, as well as the techniques developed for this analysis.

Subject headings: gamma rays: bursts — gamma rays: observations — instrumentation: polarimeters — methods: data analysis — polarization — techniques: polarimetric

Online material: color figures

1. INTRODUCTION

Despite the extensive work in recent years on GRB afterglows, the nature of the central driver that powers the burst and the prompt γ-ray emission mechanism remain enigmatic, as the physics of the afterglow is insensitive to the nature of the progenitor once a relativistic fireball is formed. There have been different suggestions for the mechanism that powers the GRB central engine. In the models invoking merging neutron stars and "collapsars" (Woosley 1993; Paczyński 1998; MacFadyen & Woosley 1999), hydrodynamically dominated outflows (jets) transport the bulk GRB kinetic energy. Alternatively, Poynting-flux may be the driver for the transport of energy to large distances (Lyutikov et al. 2003). Synchrotron radiation has traditionally been the favored emission mechanism of the prompt γ-ray emission (Mészáros et al. 1994; Tavani 1996; Dermer et al. 1999; Lloyd & Petrosian 2000), although competing Compton upscattering and synchrotron–self-Compton models have been put forward (Liang 1997; Mészáros et al. 1994; Chiang & Dermer 1999; Sari & Esin 2001; Zhang & Mészáros 2001); reviews of GRB models can be found in Piran (1999) and Mészáros (2001). In terms of polarization modeling, synchrotron radiation is naturally a strong candidate (Coburn & Boggs 2003; Granot 2003), but a portion of the polarized photon signal may also be Compton up-scattered (Eichler & Levinson 2003). A definite measurement of polarization properties from the prompt emission of GRBs will probe their anisotropy or magnetic field geometry and thereby help determine the nature of the central engine and the γ-ray emission mechanism.

The first detection of the linear polarization from the prompt γ-ray emission of a GRB indicated a very high polarization fraction of $80\% \pm 20\%$ (Coburn & Boggs 2003). For this measurement, *RHESSI* (Lin et al. 2002) data of GRB 021206 were used. The measurement demonstrated the potential for measuring polarization using Compton-scattered events between multiple detectors. Using *RHESSI*, the same method is used later to measure the polarization fraction of two X-class solar flares (Boggs et al. 2006).

The large polarization fraction obtained by Coburn & Boggs (2003) resulted in a series of theoretical work on γ-ray polarization in GRBs and Poynting-dominated flows (Lyutikov et al. 2003; Nakar et al. 2003; Eichler & Levinson 2003; Granot 2003; Dai 2004; Lazzati et al. 2004). However, independent analyses of the *RHESSI* data by other groups were not able to confirm this result at the same level of significance (Wigger et al. 2004; Rutledge & Fox 2004), so the degree of polarization for GRB 021206 remains uncertain. Clearly, more measurements, using different instruments and techniques, are required. Recently, using the BATSE instrument on *CGRO*, Willis et al. (2005) provided evidence for large polarization fractions for two bursts, GRB 930131 ($\Pi > 35\%$) and GRB 960924 ($\Pi > 50\%$), without strongly constraining the upper limits. In their work, the mass model of BATSE along with a mass model of the Earth's atmosphere were used, and the polarization fraction was determined by analyzing the angular distribution of photons that are scattered through the Earth's atmosphere. The SPI (Spectrometer on *INTEGRAL*; Vedrenne et al. 2003) and IBIS (Imager on Board the *INTEGRAL* Satellite; Ubertini et al. 2003) instruments can also measure the polarization fraction and angle of a source using the coincidence events between detector pairs (Lei et al. 1997; Kalemci et al. 2004), similar to the method employed by Coburn & Boggs (2003) and Boggs et al. (2006) with *RHESSI*.

In this letter, we discuss methods to measure polarization using one of the instruments on *INTEGRAL*, SPI, and apply these methods to measure the polarization properties of GRB 041219a, a bright and a long (about 450 s) GRB that was detected with the *INTEGRAL* Burst Alert System (IBAS) and with the *INTEGRAL* Soft Gamma-Ray Imager (ISGRI) on December 19 at 01 : 43 UT. The burst is in the fully coded field of view of both the ISGRI and

[1] Sabanci University, Orhanli-Tuzla, İstanbul, 34956, Turkey.
[2] Space Sciences Laboratory, University of California, Berkeley, CA.
[3] Department of Physics, University of California, Berkeley, CA.
[4] National Space and Technology Center, Huntsville, AL.
[5] NASA Marshall Space Flight Center, Huntsville, AL.
[6] Universities Space Research Association.
[7] Department of Physics and Astronomy, Rice University, Houston, TX.

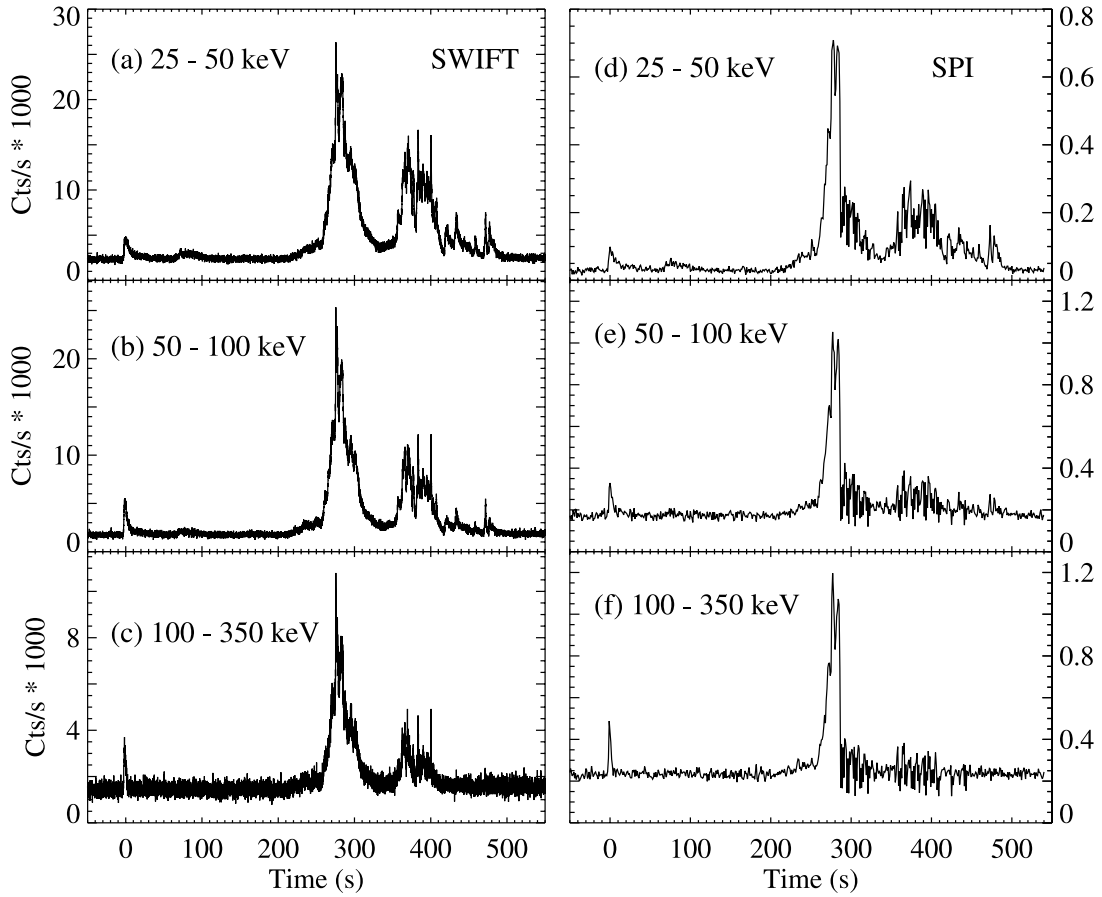

FIG. 1.—*Swift* light curves of GRB 041219a in (*a*) 25–50 keV, (*b*) 50–100 keV, and (*c*) 100–350 keV bands (Barthelmy et al. 2004), and the SPI light curves for the singles in the same bands in (*d*), (*e*), and (*f*), respectively. Times are relative to the peak of the precursor.

the SPI and is $\sim 3^\circ$ off the *X*-axis, and 155° in azimuth from the *Y*-axis.[8] The ISGRI coordinates are reported as R.A. $= 6.1075^\circ$, and decl. $= +62.8349^\circ$ with an uncertainty of $2'$ (Gotz et al. 2004). The brightest part of the burst saturated the available telemetry of *INTEGRAL*. The long duration and brightness allowed for multiwavelength campaigns for this GRB (Blake & Bloom 2004a, 2004b; Soderberg & Frail 2004; Sonoda et al. 2004). The infrared counterpart location is given as R.A. $= 6.1153^\circ$, and decl. $= 62.8426^\circ$ (Blake & Bloom 2004b). The burst was also detected with the *Swift* Burst Alert Telescope (BAT; Barthelmy et al. 2004; Fenimore et al. 2004). A comprehensive spectral and temporal analysis of the burst with SPI, *Swift* BAT, and the *RXTE* All-Sky Monitor is given in McBreen et al. 2006. The *Swift* BAT and SPI (singles) light curves are shown in Figure 1. These light curves indicate that the spectrum softens as the burst progresses and also show a precursor ~ 250 s before the main peak.

2. ANALYSIS

2.1. *SPI and γ-Ray Polarization*

SPI is a coded-aperture telescope using an array of 19 cooled germanium detectors for high-resolution spectroscopy (Vedrenne et al. 2003). It works in the 20 keV–8 MeV band and has an energy resolution of ~ 2 keV below 500 keV. The fully coded field of view is 16°, and the angular resolution is $\sim 3^\circ$. At the time of the observation, 17 detectors were active due to the failures of detectors 2 and 17 in orbit. If a photon deposits all of its energy into one detector, SPI records this as a single event. If a photon interacts through Compton scatterings with energy deposits in more than one detector, the detector and channel information for each interaction are saved into a multiple event (ME). Even though SPI is not primarily designed for polarization measurements, these ME data are inherently sensitive to polarization as linearly polarized gamma-rays preferentially scatter in azimuthal directions perpendicular to their electric polarization vector (Kalemci et al. 2004).

The two main parameters that determine the sensitivity of a multidetector instrument to gamma-ray polarization are the effective area to the multiple-detector scatter events and the average value of the polarimetric modulation factor Q, which is the maximum variation in the azimuthal scattering probability for polarized photons (Novick 1975; Lei et al. 1997). This factor is determined by the scattering cross sections,

$$Q = \frac{(d\sigma_\perp - d\sigma_\parallel)}{(d\sigma_\perp + d\sigma_\parallel)}, \quad (1)$$

where $d\sigma_\perp$ and $d\sigma_\parallel$ are the Klein-Nishina differential cross sections for Compton scattering perpendicular and parallel to the polarization direction, respectively, which are functions of the incident photon energy and the Compton scatter angle between the incident photon direction and the scattered photon direction.

[8] In this work, the azimuthal angles are defined in a plane perpendicular to the SPI pointing *X*-axis and measured with respect to the SPI *Y*-axis toward the SPI *Z*-axis.

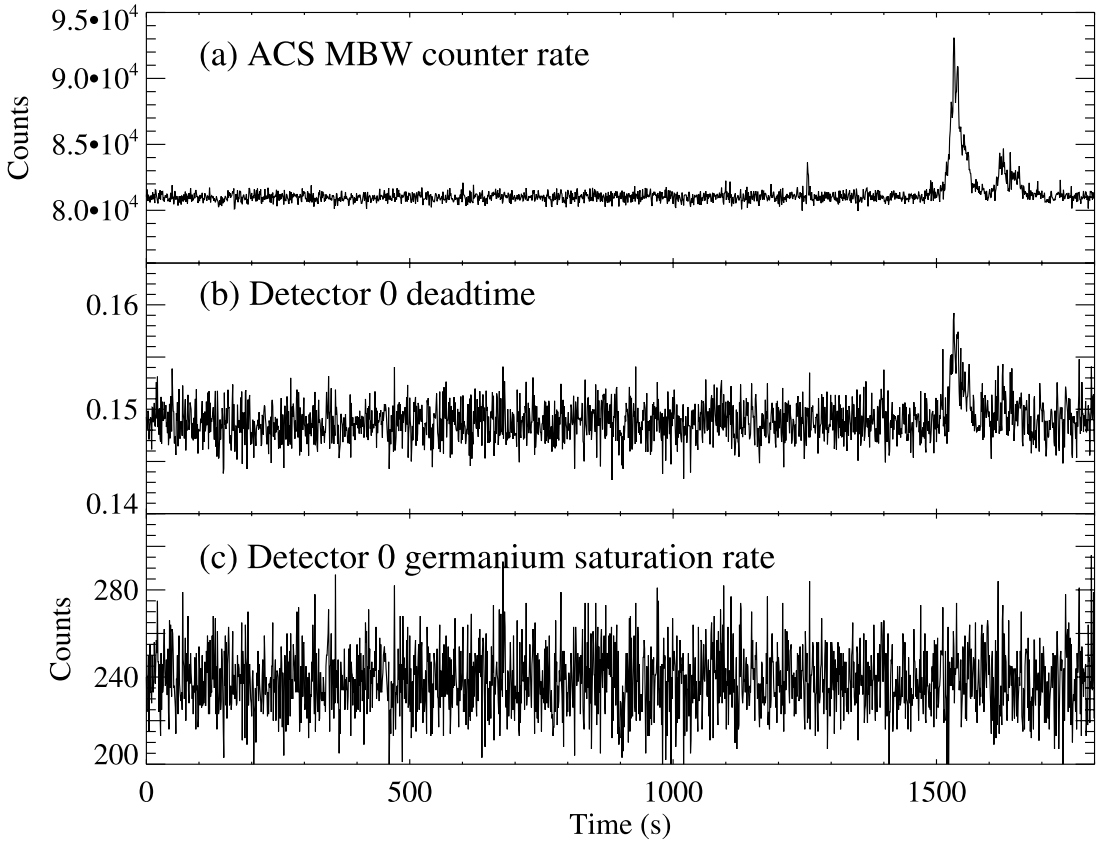

FIG. 2.—(*a*) ACS MBW counter rate, (*b*) detector 0 dead time, and (*c*) detector 0 germanium saturation rate. Time 0 is the beginning of pointing.

For a source count rate of S, and fractional polarization of Π_s, the expected azimuthal scattering angle (ϕ) distribution is

$$\frac{dS}{d\phi} = \frac{S}{2\pi}[1 - Q\Pi_s \cos 2(\phi - \eta)]. \quad (2)$$

Therefore, the "signature" of polarization is a 180° periodic modulation in the distribution of azimuthal scattering angles, with a minimum at the polarization angle η.

2.2. *GRB 041219a SPI Data*

A first look at the light curve showed that the SPI data for this GRB were affected by the telemetry saturation problems that also affected the IBIS data (Gotz et al. 2004). Figure 1 shows the SPI light curves (*right block*) for singles for the sum of all detectors. Here we define "singles"—all single detector events—as the sum of all SE and PSD events in the Integral Science Data Center (ISDC) format. As the flux peaks, a sudden drop occurs in the count rate, which was not observed in the *Swift* light curves (*left block*).

We inspected several housekeeping parameters to verify that the origin of the problem is not something other than telemetry saturation. The anticoincidence system rate, the dead time, and the germanium saturation rate for detector 0 are shown in Figure 2. Even though there is an increase in dead time, the increase is modest and cannot account for the dropouts in SPI light curves. The germanium saturation rate shows no significant deviation from the norm that could cause a sudden decrease in the count rate. We then compared the "raw" and the "prp" on-board time (processed through a standard pipeline at the ISDC) and found that the prp times have gaps that are approximately multiples of 0.125 s, indicating that telemetry packets are missing (S. Schanne 2005, private communication). Since the time and duration of the gaps are known, an approximate light curve can be reconstructed. The 100–500 keV (total energy) light curve of MEs, corrected for effective dead time due to the missing packets, is shown in Figure 3. Characterizing this effective dead time is important in terms of determining the correct background rate for the regions with the packet loss problem.

2.3. *MGEANT Simulations*

To determine the polarization fraction for this GRB, we need to compare the measured azimuthal scattering angle distribution

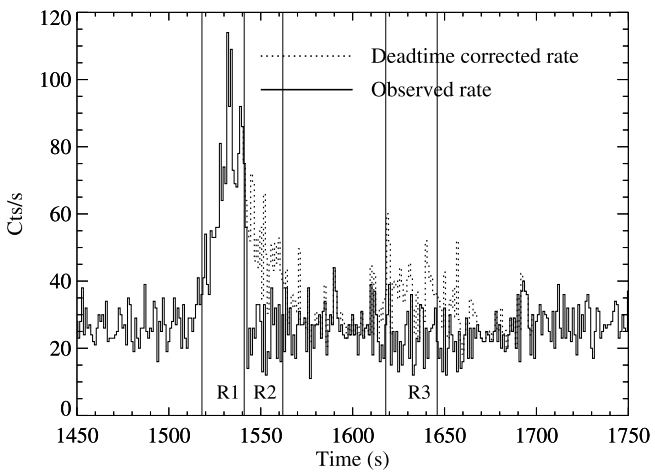

FIG. 3.—Observed (*black histogram*) and the reconstructed (*dotted histogram*) light curve of MEs in the 100–500 keV band. The gaps are treated as dead time. The vertical solid lines separate R1, R2, and R3 regions (see text). [*See the electronic edition of the Supplement for a color version of this figure.*]

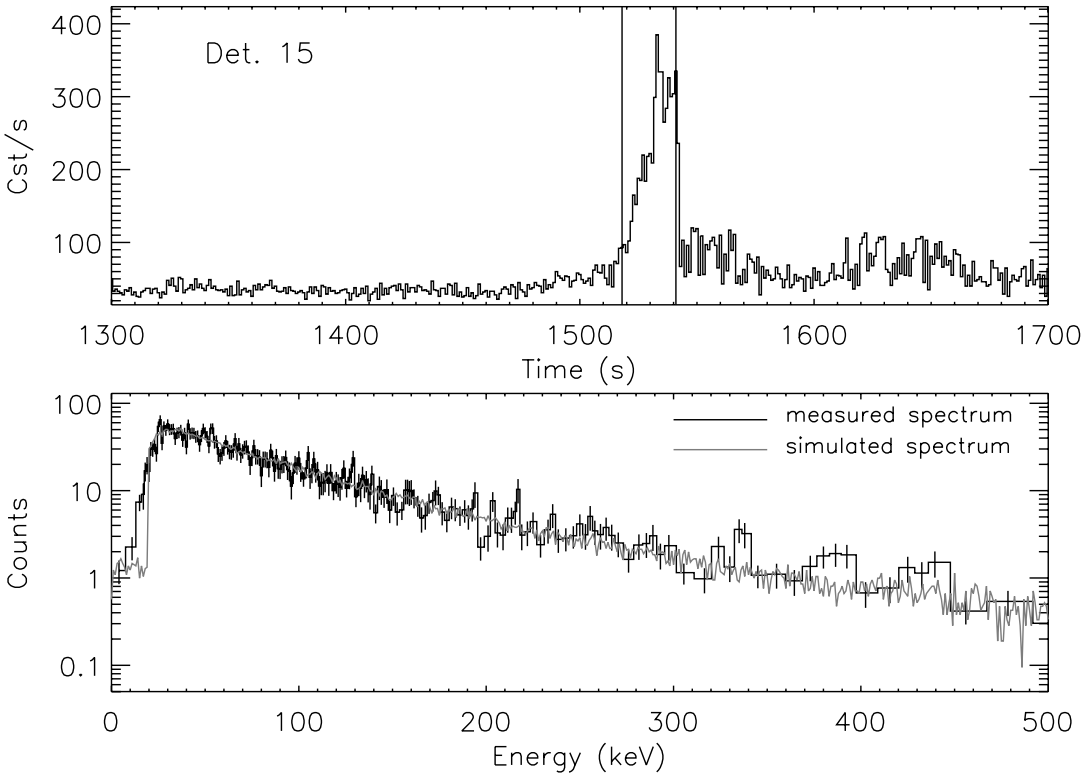

FIG. 4.—Top panel shows the singles light curve of detector 15 in the 30–490 keV band. No dead time correction is applied. The solid vertical lines indicate the region (R1) for which the spectrum is extracted. The bottom panel shows the measured (*black histogram*) and the simulated (*gray histogram*) spectrum. [*See the electronic edition of the Supplement for a color version of this figure.*]

to the expected distribution for an unpolarized and a polarized source from this sky location. The only method available for performing this comparison is with detailed Monte Carlo simulations. The response to a polarized source is characterized by the polarimetric modulation factor, Q, discussed in § 2.1. Since Q is energy-dependent, it will depend on the energy spectrum of the source. We therefore used simulations for two purposes: to obtain the spectral parameters (§ 2.4) and to obtain the modulation factors.

The simulations are performed using MGEANT (Sturner et al. 2000), which is a γ-ray instrument simulation package developed at NASA GSFC. The MGEANT source code allows several beam geometries and spectra to be specified at compile time. A highly detailed SPI mass model is used as an input to MGEANT. In order to have a complete response, the mass model of the rest of the spacecraft (Ferguson et al. 2003) is also included. This mass model is the same as the mass model used to create SPI response matrices with MGEANT. More information on MGEANT and the complete mass model we used can be found in Sturner et al. (2003).

2.4. *GRB 041219a Spectrum*

Detailed and precise determination of the GRB 041219a spectral parameters is not necessary for this work, as Q is not strongly dependent on the exact spectral parameters. Therefore, a rough determination of the GRB spectrum is adequate for our study. To determine the spectral parameters, we first obtained the singles count spectrum from the region with no packet loss (R1 in Fig. 3). We determined the background for each detector as follows: We took the data from the first 1000 s from the beginning of the pointing and obtained a spectrum. Next we applied two corrections. We fitted the background light curve with a first order polynomial to take into account a small (a few percent) and gradual increase toward the GRB. Second, we found the live times at the background region ($B_{\rm livetime}$) and the GRB region ($\rm GRB_{livetime}$) and multiplied the background spectrum with $\rm GRB_{livetime}/B_{livetime}$. An example spectrum after background subtraction is shown in Figure 4.

After the photons from the GRB event were isolated and spectra for each detector were obtained, the next step is to reproduce these spectra with simulations. To perform the simulations, we first modified the original mass model such that the detectors 2 and 17 are not active. We obtained longitude and latitude of the spacecraft axes using `spipoint` and used the position of the infrared counterpart for the GRB. We ran three simulations with the Band Function (Band et al. 1993) spectrum using (1) $\alpha = 1.0$, $\beta = 2.4$, $E_{\rm br} = 170$; (2) $\alpha = 1.0$, $\beta = 2.0$, $E_{\rm br} = 170$; and (3) $\alpha = 1.0$, $\beta = 2.0$, $E_{\rm br} = 200$.

For simplicity, the mass model uses a single mass for all detectors, even though in reality the mass of each detector is slightly different. This mass distribution causes the largest detector-to-detector variations in efficiency (Sturner et al. 2003). The simulated spectra were corrected for this effect. We also applied a correction for dead time for each detector. Apart from these detector-dependent corrections, there are also detector-independent corrections regarding the photo-peak efficiencies and the mask transmission. These were also applied as described in Sturner et al. (2003). We found that the spectrum with this set of parameters, $\alpha = 1.0$, $\beta = 2.0$, and $E_{\rm br} = 200$, best describes the data in R1. In Figure 4, we show the actual and the simulated spectrum of detector 15 as an example.[9]

We also checked the detector distribution of 30–490 keV band total singles counts and compared it to the simulated distribution.

[9] These spectral results were obtained before the publication of McBreen et al. (2006). Even though the band function parameters are different, the effect of small differences in the energy spectrum is not important for polarization measurements.

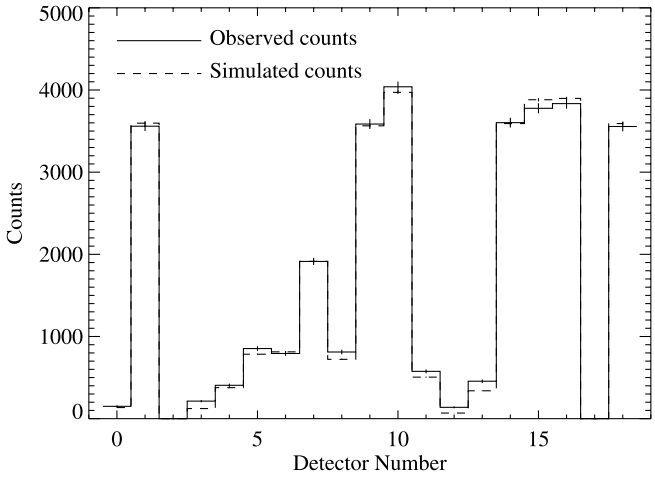

FIG. 5.—Comparison between the actual (*solid histogram*) and the simulated (*dashed histogram*) number of counts for each detector for singles, in the 30–490 keV band.

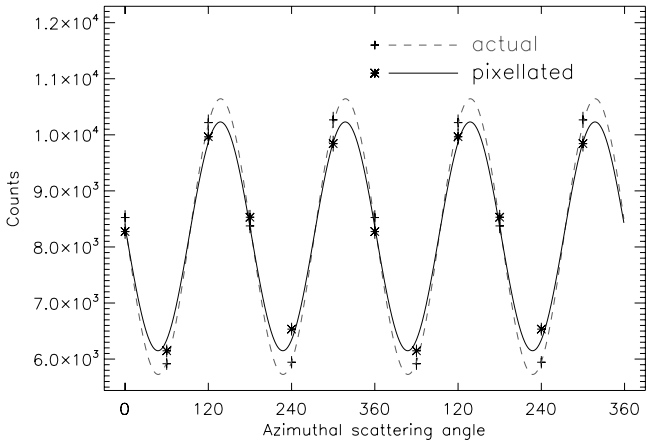

FIG. 6.—Simulated azimuthal scattering angle distribution of 100% polarized photons at 200 keV originating at the GRB position. The center-to-center pixellated distribution (*black fit*) has lower modulation amplitude than the distribution obtained using interaction positions within the detectors (*dashed fit*). [*See the electronic edition of the Supplement for a color version of this figure.*]

The result is shown in Figure 5. The simulation (*dashed lines*) reproduced the actual distribution well (within a few percent) for detectors not shadowed by the mask. For the detectors under the shadow of the mask elements, the discrepancy is larger if expressed in percentage. Note that the number of events in these detectors is much less than in the open detectors. Finally, we compared the total number of MEs after cuts (see § 3) with the total number of MEs from simulations. We obtained 534 MEs from simulations compared to 543 events from the data, an agreement within 2%.

Overall, the Band spectrum with $\alpha = 1.0, \beta = 2.0, E_{\rm br} = 200$, represents the GRB in R1, and the simulation reflects the actual detector to detector distribution.

2.5. *Modulation Factor*

The next step to measure polarization is to obtain Q (see eq. [1]) by comparing the azimuthal scattering angle distributions of nonpolarized and 100% polarized photons. Both can be created using MGEANT simulations. Determining the azimuthal scattering angle requires finding the direction of the photon as it scatters from one detector to the other. SPI records the energies and the detectors in a ME. However, the direction of the photon cannot be uniquely determined for all events. The conservation of energy and momentum in the Compton scattering process place limits on the energies deposited in each detector. Assuming full energy deposition in two detectors after a single Compton scattering,

$$\frac{m_e c^2}{E_1} - \frac{m_e c^2}{E_1 + E_2} = 1 - \cos(\theta), \qquad (3)$$

where E_1 is the energy deposition in the first detector, E_2 is the energy deposition in the second detector, and m_e is the mass of the electron. One can easily show that for relatively small total energies $[E_1 + E_2 \leq (m_e c^2)/2]$ E_2 is always greater than E_1. As the initial energy increases, the number of cases with $E_2 < E_1$ increases, and finally at $m_e c^2 = 511$ keV, there is equal probability for either case. For the spectrum of GRB 041219, most of the photons Compton scattered from the low-energy deposition detector to the high-energy deposition detector. Therefore, we tag the direction of every photon as originating from the lower energy deposition detector. Even though some of the interactions will be tagged incorrectly this way, the final results should not be affected significantly due to the 180° symmetry of the polarization modulations.

On the other hand, MGEANT simulations provide more information than that of the real data. First, in simulations, the interaction positions within the individual detectors are known. Second, for any incoming photon energy, the direction of the photon is also known. We determined azimuthal scattering angle distributions for three cases: (a) using the actual interaction positions and directions determined by the simulation; (b) using the detector center-to-center angles (pixellation) and directions determined by the simulation; and (c) using the center-to-center angles and directions determined using energy depositions. Cases a and b can only be calculated using the simulations, and case c represents distribution for the actual data.

We obtained the modulation factors by following the method described in Lei et al. (1997). For the simulated events with 100% polarized photons ($\Pi_s = 1$) the modulation factor can be obtained by fitting the azimuthal scattering angle distribution with a $\cos 2(\phi - \eta)$ function (see eq. [2]). However, before doing this, one needs to take into account the "response" of the distribution for nonpolarized photons. This response is obtained by dividing the nonpolarized simulated azimuthal scattering angle distribution by its average. We divided the 100% polarized azimuthal scattering angle distribution with this response. For the response we use, the modulation is on top of an average rate.

Figure 6 shows the azimuthal scattering angle distribution of 100% polarized photons at 200 keV as an example. The amplitude of the modulation with respect to the average gives the modulation factor. The pixellation reduces the modulation factor around 20% (with respect to nonpixellated modulation) at 200 keV.

We ran more simulations with monoenergetic photons at different energies, with nonpolarized and 100% polarized photons, with a randomly chosen polarization angle of 45°. Then we histogrammed the azimuthal scattering angles using three different methods described earlier. Figure 7 shows the distribution of modulation factor as a function of energy for different cases. The ~3° off-axis position of the GRB and the reduced number of detectors did not affect the modulation factors significantly. More importantly, using the energy depositions to determine the directions rather than using the actual directions has no effect on the modulation factor.

Finally, by using simulations with the GRB spectrum described above, we determined the modulation factor for R1 in the 100–350 keV band. We ran the simulations with different polarization

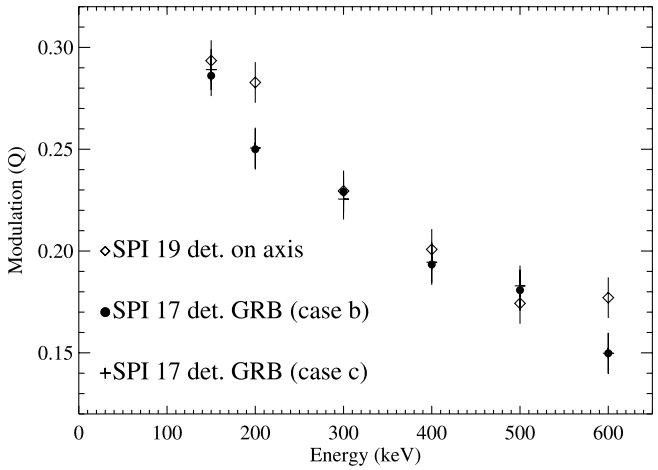

FIG. 7.—Simulated modulation factors as a function of energy for three cases; diamonds represent the hypothetical case of an on-axis GRB (with the same spectra of GRB 041219) with 19 detectors on, using the actual directions from simulations (case b), filled circles and crosses represent the known position of GRB 041219a with 17 detectors, with cases b, and c, respectively (see text for more explanation on each case). All three cases are pixellated.

angles. The results are shown in Figure 8. For the pixellated case, Q varies between 18% and 21%. The average modulation is 20%. With real interaction positions and order, the distribution shows a similar behavior, varying between 23% and 26% with an average of 25%. Similar to monochromatic tests, the pixellation reduces the average modulation factor 20% for the GRB position and spectrum.

2.6. *Search for Systematic Effects*

Since *INTEGRAL* is not rotating, systematic effects not foreseen by the simulations could alter the azimuthal scattering angle distribution. Even though we apply corrections to the simulations, there may be systematic effects related to ME events that are not discussed in Sturner et al. (2003). We therefore analyzed some of the data taken at the ground calibration tests of SPI (the Bruyères–Le-Châtel data set; Attié et al. 2003) to search for systematic effects that could affect polarization measurements. The best calibration data set for our purposes is the case with no mask, on-axis, and

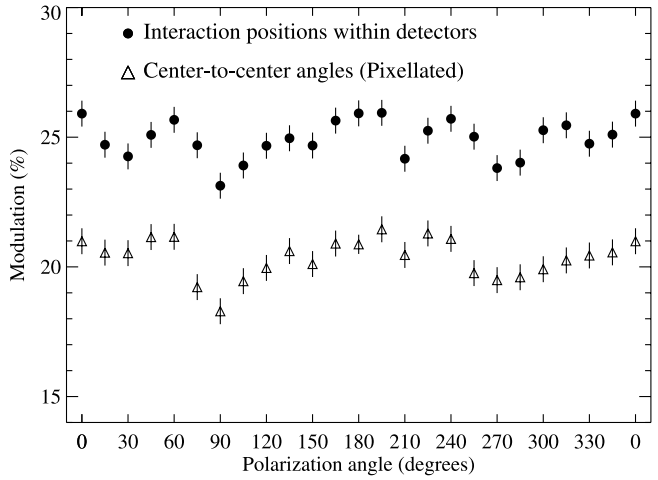

FIG. 8.—Simulated modulation factors for GRB 041219a (100–350 keV) as a function of polarization angle. Interaction positions within detectors are used to obtain the points shown with circles. The triangles, on the other hand, uses center-to-center angles. Our best-fit determination of the input spectrum during R1 is used.

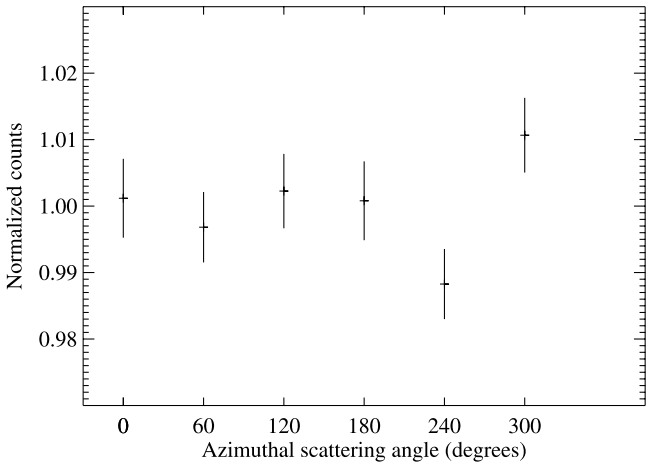

FIG. 9.—Azimuthal scattering angle distribution of a calibration run with no mask. The histogram is divided by its average to obtain variations with respect to the mean. The variations are in the 1% level.

using ^{133}Ba, which resulted in strong lines at 276.4, 302.9, and 356.0 keV. Unfortunately, after the runs, it was discovered that the source position was slightly offset. A Hostaform plastic device inserted in the center of the plastic anticoincidence scintillator shadows detector 0. Due to the offset, it also cast a shadow on detectors 2 and 3. We decided to ignore all interactions between detector 0 and the surrounding six nearest neighbor detectors for this analysis. We also excluded the interactions that involve detectors 2 and 17, as they are no longer operational. We only used the interactions for which the total energy gives the line energy. We did not apply a dead time correction, but applied a correction factor to account for differing detector masses (see § 3). Then we ran our standard histogram procedures to obtain the azimuthal scattering angle distribution. Figure 9 shows this distribution normalized by its average. The variations are in the 1% level. Therefore, excluding interactions in detector 0, the systematic errors inherent to the detectors are of the order of 1%.

2.7. *Chance Coincidences*

An important factor in polarization experiments using coincidence events is the rate of chance coincidences, events in two detectors that occur within the predetermined coincidence window. The electronic coincidence window is 350 ns for SPI, i.e., two events in different detectors that occur within 350 ns of each other are recorded as a ME. At the peak of the outburst, the total count rate in singles for the detectors that are not shadowed is $\sim$400 counts s^{-1}. When we eliminate pairs that will not obey our selection criteria (see § 3), the maximum singles count rate for each detector is $\sim$150 counts s^{-1}. Therefore, the maximum chance coincidence rate at the peak of the outburst is only 0.008 counts s^{-1} per detector pair, which is negligible for our measurements.

3. POLARIZATION MEASUREMENT

Before analyzing the data, we applied three energy cuts to the multiple events: the minimum allowed energy for each detector in a pair is 26 keV, the minimum allowed total energy of a pair is 100 keV, and the maximum allowed total energy of a pair is 350 keV. The minimum cuts are necessary to ensure that the events are actual Compton events. They also cut a significant portion of small Compton scattering angles that contribute less to the modulation factor. The maximum cut is required for two reasons. First, due to low count rates and low modulation factors, including the very high-energy part does not improve the measurement.

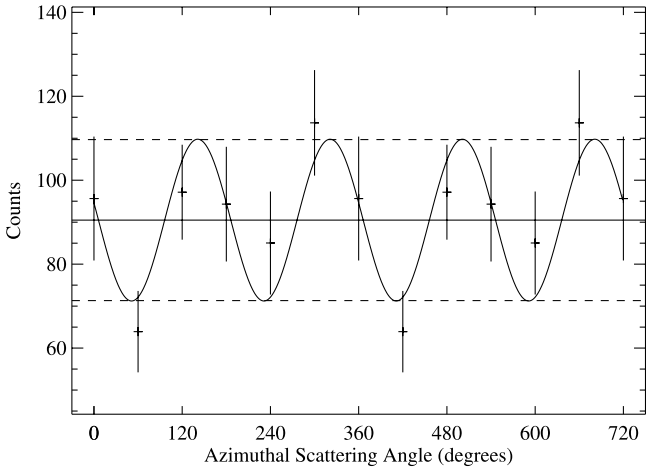

FIG. 10.—Azimuthal scattering angle distribution of events in region 1 and a $\cos 2(\phi - \eta)$ fit to the data. The solid line shows the average (no polarization), and the dashed lines show the maximum and the minimum modulation for a 100% polarization fraction.

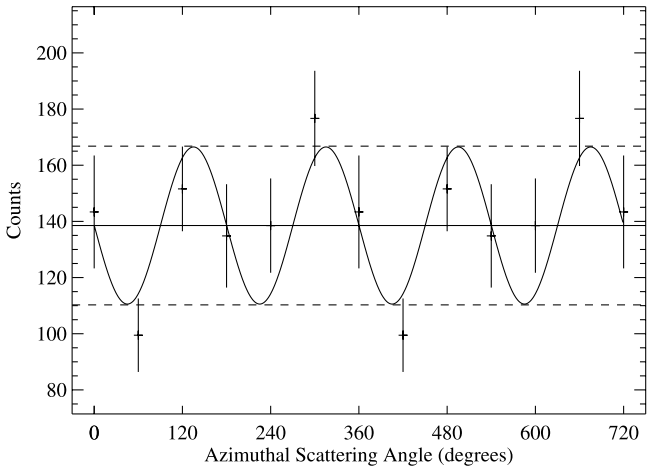

FIG. 11.—Azimuthal scattering angle distribution of events in regions 1, 2, and 3 and a $\cos 2(\phi - \eta)$ fit to the data. The solid line shows the average (no polarization), and the dashed lines show the maximum and the minimum modulation for a 100% polarization fraction.

Second, as discussed in § 2.5, as the total energy increases, the number of events with incorrect azimuthal scattering angles increases. To obtain maximum allowed total energy we considered the signal/noise ratio of MEs for different energies, their respective modulation factors, and finally the fraction of the incorrectly tagged events. And finally, we cut all MEs with total energies between 184 and 201 keV to remove a significant number of background photons in the prominent Ge line at 198 keV.

We then defined two pseudodetectors (PDs) for each detector pair (i.e., events that scatter from detector 0 to detector 1 is PD1, and events that scatter from detector 1 to detector 0 is PD2; therefore, it is different than the pseudodetector definition of ISDC). We only used the nearest neighbors. Even though it is possible to increase the number of angles by using non-neighbor detectors, the number of these events are too low to include in the analysis. There are 64 PDs after the failures of detector 2 and 17.

We separated the light curve into three regions. Region 1 is from the beginning of the burst to the time that the packet-loss problems began. Region 2 and region 3 are determined using the source and background rates to maximize the source-to-background ratio. These regions are denoted as R1, R2, and R3 in Figure 3. The analysis is relatively straightforward for R1. For each PD, the background is determined exactly as determined for singles: using the first 1000 s of the pointing. The rate is again corrected for dead time and evolution. The total-background counts are histogrammed into 6 azimuthal scattering angles. The total number of source counts is 545, and the total number of background counts is 171.

The simulated, nonpolarized events are corrected for mass and dead time. The dead time for a pair is calculated using both the dead time due to ACS vetos and the detector electronics. We multiplied the number of events in PDs with $(m_1 + m_2)/2m_{\rm avg}$, where m_1 and m_2 are masses of the detectors that form the PDs and $m_{\rm avg}$ is the average mass of all detectors. After these corrections, we histogrammed the simulated data exactly as we histogrammed the real data. To obtain the polarization fraction, we followed the method described in Lei et al. (1997) and also discussed in § 2.3. The resultant distribution and the $\cos 2(\phi - \eta)$ fit are shown in Figure 10. The best-fit modulation amplitude is $Q\Pi_s = 21.3\% \pm 7.6\%$, corresponding to a polarization angle $\eta = 48.3^\circ \pm 3.8^\circ$. The χ^2 for this best fit is 2.69 for 3 degrees of freedom (dof). For comparison, the χ^2 for the best fit assuming no polarization (flat distribution) is 11.00 for 5 dof. For polarization angles $\eta \sim 45^\circ$, we calculate the polarimetric modulation factor as $Q = 21.2$ (Fig. 8). Correcting the best-fit modulation amplitude for this factor yields a best-fit polarization amplitude of $\Pi_s = 100\% \pm 36\%$, providing no upper bound.

We tried to obtain better constraints by combining regions 1, 2, and 3. For regions 2 and 3, we determined the additional dead time due to the missing packets and corrected the background according to this dead time. The remainder of the analysis is the same as region 1. For the combined case (R1 + R2 + R3), the source counts and background counts are 839 and 389, respectively. Because of the evolution of the GRB spectra, the combined spectrum is slightly softer than the spectrum of R1. We determined that a Band function with $\alpha = 1.15$, $\beta = 2.4$, and $E_{\rm br} = 180$ fits the overall spectrum well.

The azimuthal scattering angle distribution for the combined case is shown in Figure 11. The fit shown yields a modulation amplitude of $Q\Pi_s = 20.2\% \pm 6.7\%$ with a minimum at $45.4^\circ \pm 5.2^\circ$. The modulation factor at this angle is 20.4%, corresponding to $\Pi_s = 99\% \pm 33\%$. The χ^2 for the $\cos 2(\phi - \eta)$ fit is 4.68 for 3 dof, whereas the χ^2 for the flat distribution is 15.10 for 5 dof. Neither of these fits represent the data well, as seen in Figure 11, and as also inferred from the χ^2 values. Given our measurement uncertainties, and assuming an unpolarized (flat) distribution, a simple Monte Carlo simulation yields the chance probability of fitting a modulation of this amplitude as 1.01%. The best-fit polarization yields a lower reduced χ^2 over the fit assuming no polarization, with an *F*-test (Bevington & Robinson 1992) value of 3.34 with 17.3% chance probability (over a flat distribution).

4. DISCUSSION

We have demonstrated techniques to measure polarization of the prompt γ-ray emission of a GRB in the field of view of SPI on *INTEGRAL*. However, for GRB 041219a, we have not strongly constrained models for the emission mechanism nor for the central engine. The ME count rate is not high enough for statistically significant measurements. For comparison, the *RHESSI* solar flare polarization measurements use approximately 6500 counts and 16,000 counts for two flares (Boggs et al. 2006), and we use only 839 source counts for GRB 041219a.

Another problem is the dependence of the polarization fraction on energy cuts. The quoted numbers in this work are for the

cases with the largest polarization fractions with the highest F-test values compared to a flat distribution. However, choosing different energy bands for minimum and maximum energies yields lower polarization fractions. For example, using 500 keV as the maximum total energy yields a polarization fraction of 65% $\pm$ 31%, with a minimum at 52°. We obtain significantly lower polarization fractions if the 198 keV Ge line is not filtered out. If we use energies up to 500 keV and do not cut the 198 keV line, the polarization fraction is 55% $\pm$ 30%. The polarization angle may be changing with energy, causing a decrease in the overall modulation. Unfortunately, the statistics are not good enough to test this hypothesis.

Our analysis indicates that systematic effects from the two inactive SPI detectors, as determined from preflight calibration data, should not significantly affect these polarization measurements. We do not have knowledge of any further systematic effects in orbit that could affect this polarization measurement. Analysis of more GRBs may reveal systematic effects, with the potential of distinguishing whether the high modulation we measured here was a result of high polarization fraction, a systematic effect, or just a chance fluctuation.

The packet loss problem did not play a big role in constraining the polarization parameters for this GRB. Without any packet loss, there would have been a sensitivity gain of 15%, which would not have significantly affected the upper limit determination, and may have placed a slightly more stringent lower limit. This exercise showed that SPI has a better chance of measuring polarization fraction for harder, longer bursts.

5. CONCLUSION

We have used data from SPI on *INTEGRAL*, an instrument not intended for polarization studies, and tried to constrain polarization parameters of GRB 041219a, a long and bright GRB in the field of view. The distribution of azimuthal scattering angles from GRB 041219a is better represented by a polarized source compared to a nonpolarized source, but with low statistical significance. Due to large uncertainties, we have not strongly constrained models for the emission mechanism, nor for the central engine. In order to do so, future soft γ-ray missions with polarization sensitivity should necessarily aim for an ability to measure polarizations at the 5%–10% level, preferably in 3–4 neighboring energy windows, and also 2–4 intervals spanning a burst's duration. These requirements would render a γ-ray polarimeter capable of exploring energy-dependent polarization dependence around the $\nu - F_\nu$ peak and also temporal evolution of both the angle and degree of polarization. Knowledge of such source characteristics can realistically discriminate between some suggested radiation mechanisms and different model geometries that are currently being contemplated in the GRB literature.

E. K. is supported by the European Commission through a FP6 Marie Curie International Reintegration grant (INDAM, MIRG-CT-2005-017203). E. K. also acknowledges NASA grant NAG5-13142 and partial support of TÜBİTAK. M. B. acknowledges NASA grant NNG06GB81G for support. We thank Steve Sturner and Chris Schrader at GSFC for providing the BLC data, and their helps in MGEANT analysis. We also thank Volker Beckmann for his helps on the SPI GRB analysis. We thank Stephane Schanne at SACLAY for clarifying telemetry problems, and Pierre Dubath at ISDC for clarifying dead-time routines. We acknowledge Mark Kippen and Mark McConnell for the "GLEPS" package in MGEANT. E. K. thanks Dave Willis and Roland Diehl at MPE for useful discussions.

REFERENCES

Attié, D., et al. 2003, A&A, 411, L71
Band, D., et al. 1993, ApJ, 413, 281
Barthelmy, S., et al. 2004, GCN Circ., 2874, http://gcn.gsfc.nasa.gov/gcn3/2874.gcn3
Bevington, P. R., & Robinson, D. K. 1992, Data Reduction and Error Analysis for the Physical Sciences (2nd ed.; New York: McGraw-Hill)
Blake, C., & Bloom, J. S. 2004a, GCN Circ., 2870, http://gcn.gsfc.nasa.gov/gcn3/2870.gcn3
———. 2004b, GCN Circ., 2872, http://gcn.gsfc.nasa.gov/gcn3/2872.gcn3
Boggs, S. E., Coburn, W., & Kalemci, E. 2006, ApJ, 638, 1129
Chiang, J., & Dermer, C. D. 1999, ApJ, 512, 699
Coburn, W., & Boggs, S. E. 2003, Nature, 423, 415
Dai, Z. G. 2004, ApJ, 606, 1000
Dermer, C. D., Chiang, J., & Böttcher, M. 1999, ApJ, 513, 656
Eichler, D., & Levinson, A. 2003, ApJ, 596, L147
Fenimore, E., et al. 2004, GCN Circ., 2906, http://gcn.gsfc.nasa.gov/gcn3/2906.gcn3
Ferguson, C., et al. 2003, A&A, 411, L19
Gotz, D., Mereghetti, S., Shaw, S., Beck, M., & Borkowski, J. 2004, GCN Circ., 2866, http://gcn.gsfc.nasa.gov/gcn3/2866.gcn3
Granot, J. 2003, ApJ, 596, L17
Kalemci, E., Boggs, S. E., Wunderer, C. B., & Jean, P. 2004, in Proc. 5th *INTEGRAL* Workshop, The *INTEGRAL* Universe, ed. V. Schönfelder, G. Lichti, & C. Winkler (ESA SP-552; Noordwijk: ESA), 859
Lazzati, D., Rossi, E., Ghisellini, G., & Rees, M. J. 2004, MNRAS, 347, L1
Lei, F., Dean, A. J., & Hills, G. L. 1997, Space Sci. Rev., 82, 309
Liang, E. P. 1997, ApJ, 491, L15
Lin, R. P., et al. 2002, Sol. Phys., 210, 3
Lloyd, N. M., & Petrosian, V. 2000, ApJ, 543, 722
Lyutikov, M., Pariev, V. I., & Blandford, R. D. 2003, ApJ, 597, 998
MacFadyen, A. I., & Woosley, S. E. 1999, ApJ, 524, 262
McBreen, S., Hanlon, L., McGlynn, S., McBreen, B., Foley, S., Preece, P., von Kienlin, A., & Williams, O. R. 2006, A&A, 455, 433
Mészáros, P. 2001, Science, 291, 79
Mészáros, P., Rees, M. J., & Papathanassiou, H. 1994, ApJ, 432, 181
Nakar, E., Piran, T., & Waxman, E. 2003, J. Cosmol. Astropart. Phys., 10, 5
Novick, R. 1975, Space Sci. Rev., 18, 389
Paczyński, B. 1998, ApJ, 494, L45
Piran, T. 1999, Phys. Rep., 314, 575
Rutledge, R. E., & Fox, D. B. 2004, MNRAS, 350, 1288
Sari, R., & Esin, A. A. 2001, ApJ, 548, 787
Soderberg, A. M., & Frail, D. A. 2004, GCN Circ., 2881, http://gcn.gsfc.nasa.gov/gcn3/2881.gcn3
Sonoda, E., Maeno, S., Matsuo, Y., & Yamauchi, M. 2004, GCN Circ., 2882, http://gcn.gsfc.nasa.gov/gcn3/2882.gcn3
Sturner, S. J., Seifert, H., Shrader, C., & Teegarden, B. J. 2000, in AIP Conf. Ser. 510, ed. M. L. McConnell & J. M. Ryan (New York: AIP), 814
Sturner, S. J., et al. 2003, A&A, 411, L81
Tavani, M. 1996, Phys. Rev. Lett., 76, 3478
Ubertini, P., et al. 2003, A&A, 411, L131
Vedrenne, G., et al. 2003, A&A, 411, L63
Wigger, C., Hajdas, W., Arzner, K., Güdel, M., & Zehnder, A. 2004, ApJ, 613, 1088
Willis, D. R., et al. 2005, A&A, 439, 245
Woosley, S. E. 1993, ApJ, 405, 273
Zhang, B., & Mészáros, P. 2001, ApJ, 559, 110